Onboard Generation of Three-Dimensional Constrained Entry Trajectories

Zuojun Shen* and Ping Lu†
Iowa State University, Ames, Iowa 50011-2271

A methodology for very fast design of three-degree-of-freedom (3DOF) entry trajectories subject to all common inequality and equality constraints is developed. The approach makes novel use of the quasi-equilibrium glide phenomenon in lifting entry as a centerpiece for effective and efficient enforcement of the inequality constraints. The highly constrained nonlinear trajectory planning problem is decomposed into two sequential one-parameter search problems. The algorithm is able to generate a complete and feasible 3DOF entry trajectory of 25-min flight time in about 2–3 s on a desktop computer, given the entry conditions, values of constraint parameters, and final conditions. High-fidelity numerical simulations with a reusable launch vehicle model for various entry missions and trajectory planning using the space shuttle model are presented to demonstrate the capability and effectiveness of the algorithm.

I. Introduction

ENTRY flight is a critical phase of operation for any reusable launch vehicle (RLV), crew return vehicle (CRV), or cargo transfer vehicle (CTV). The entry guidance system determines the necessary commands to control the trajectory during entry. The benchmark in entry guidance is the space shuttle entry guidance design.[1] The shuttle entry guidance consists of two parts: offline planning of a reference drag–acceleration profile and onboard tracking of the drag profile. The planning of the drag profile is based on longitudinal considerations, the range requirement in particular, and the need for satisfying inequality trajectory constraints. The magnitude of bank angle is determined by tracking the drag profile, whereas its sign is determined by a preselected heading error corridor criterion. For a given drag profile, this corridor can be chosen so that the vehicle achieves a correct heading relative to the landing site. To compensate for dispersions, the reference drag profile can be adjusted inflight according to the current condition to null range errors. This adaptive capability is important to the range precision of the shuttle-type entry guidance methods.

Although the shuttle entry guidance is highly successful, the search has been continued for entry guidance methods that enable fully autonomous and adaptive entry guidance. A key requirement for such a system is to not rely on a reference trajectory generated on the ground. With regard to this requirement, the predictor–corrector methods aim at iteratively determining trajectory controls online for a trajectory leading from the current condition to the target condition. These types of methods have been examined in a number of applications.[2−4] Because repeated integrations of the equations of motion are involved, simple parameterization of the control histories is typically used for the problem to be solvable in an onboard environment. Further development of this class of methods should address the lack of effective mechanism to enforce strictly various inequality trajectory constraints[5] that are critically important in

entry flight. Seeking to maintain the strong attributes of the shuttle entry guidance, Mease et al. propose a fast entry trajectory planning method in which the reference trajectory is still based on the drag profile.[6] However, the design of the reference drag profile takes into simultaneous consideration both downrange and crossrange requirements in three-dimensional flight. Roenneke, on the other hand, looks for ways to obtain optimal drag profiles quickly, based on the downrange requirement for onboard implementation.[7] Once the reference drag profile is generated, the rest of the steps would be similar to shuttle entry guidance. Girerd and Barton develop an approach to determine onboard the subsonic drop test trajectories for the X-34 experimental vehicle.[8] The algorithm simultaneously designs an altitude-vs-range profile and a ground track using geometric segments and a trajectory selection criterion based on the rate of the dynamic pressure.

An entry guidance system that can autonomously design the reference trajectory would give rise to several benefits unmatched by the current system. It would allow autonomous aborts of the RLV from any recoverable entry condition resulting from aborts during ascent or abnormality during entry. In the event of in-orbit contingency, the CRV/CTV may initiate entry at moment's notice to land at the first available landing site without having to wait for the guidance updates from the ground. Should a system failure occur during normal entry flight that necessitates landing at an alternate site, the guidance system would be able to determine where to go and to generate all of the required guidance commands. This entry guidance system would also require significantly less premission analysis and planning for different missions and, thus, reduce dramatically the reoccurring operational costs associated with entry guidance.

Under the current NASA Space Launch Initiative program, autonomous adaptive entry guidance methods are being closely examined. An ideal algorithm for planning the entry trajectory onboard should have a number of key ingredients: guaranteed satisfaction of all of the inequality constraints, reliability, efficiency, flyability of the trajectory, and accuracy in meeting all of the specified terminal conditions. To be effective in the downrange as well as the crossrange channel, and applicable to different vehicles in different mission scenarios with different requirements, the algorithm should consider both longitudinal and lateral motions in the trajectory design process, as is done in Refs. 6 and 8. One of the considerations taken into account in the shuttle entry guidance using drag acceleration as the tracking reference was inaccuracy in geometric altitude data from the inertial navigation system. With the availability of more accurate navigation systems such as the global positioning system, navigation limitations are no longer an obstacle. Henceforth, we believe that planning the trajectory directly in the natural state space of three-degree-of-freedom (3DOF) motion can best accommodate all of the possible trajectory constraints and targeting

*Graduate Research Assistant, Department of Aerospace Engineering and Engineering Mechanics; currently Postdoctoral Research Associate, Department of Aerospace Engineering and Engineering Mechanics, Iowa State University, Ames, IA 50011-2271; zjshen@iastate.edu.

†Associate Professor, Department of Aerospace Engineering and Engineering Mechanics; plu@iastate.edu. Associate Fellow AIAA.

conditions and ensure the flyability of the reference trajectory. Such a reference trajectory provides the most complete information for guidance. When this 3DOF reference trajectory is tracked closely, the actual entry trajectory will meet all of the requirements.

This paper presents an approach for onboard entry trajectory generation in the aforementioned direction. The algorithm, however, is completely new and conceptually different from the ones investigated previously. A chief difficulty in planning 3DOF entry trajectories onboard is ensuring the strict satisfaction of all of the path (inequality) trajectory constraints. Even in offline trajectory planning, the commonly employed methods will inevitably require many iterations. Oftentimes it needs to be "tweaked" by an experienced engineer for the process to achieve convergence. The centerpiece in our algorithm for addressing this key issue is the novel use of a quasi-equilibrium glide condition. With the aid of this condition, we are able to reduce the infinite-dimensional problem of meeting the path constraints and establishing the longitudinal trajectory profiles into a one-parameter search problem. The lateral trajectory profiles are then obtained by another one-parameter search problem in which the point of a bank angle reversal is found. The algorithm ensures that the trajectory is flyable because the trajectory and controls satisfy the equations of motion with the vehicle aerodynamic modeling, and the control authority constraints in terms of rates and accelerations are enforced. A considerable number of entry missions using the vehicle data of the X-33 and the shuttle are tested with this algorithm. The algorithm is able to generate a fully constrained 3DOF flyable trajectory within 2–3 s on a desktop computer in all cases. The effectiveness and performance of the combined entry guidance of the trajectory generation algorithm and the trajectory tracking are demonstrated with high-fidelity dispersion simulations.

II. Fundamentals

A. Entry Dynamics

The 3DOF point-mass dynamics of the RLV over a spherical rotating Earth are described by following dimensionless equations of motion[9]:

$$\dot{r} = V \sin \gamma \tag{1}$$

$$\dot{\theta} = V \cos \gamma \sin \psi / r \cos \phi \tag{2}$$

$$\dot{\phi} = V \cos \gamma \cos \psi / r \tag{3}$$

$$\dot{V} = -D - (\sin \gamma / r^2) + \Omega^2 r \cos \phi (\sin \gamma \cos \phi$$
$$\quad - \cos \gamma \sin \phi \cos \psi) \tag{4}$$

$$\dot{\gamma} = (1/V)[L \cos \sigma + (V^2 - 1/r)(\cos \gamma / r) + 2\Omega V \cos \phi \sin \psi$$
$$\quad + \Omega^2 r \cos \phi (\cos \gamma \cos \phi - \sin \gamma \cos \psi \sin \phi)] \tag{5}$$

$$\dot{\psi} = (1/V)[L \sin \sigma / \cos \gamma + (V^2/r) \cos \gamma \sin \psi \tan \phi$$
$$\quad - 2\Omega V (\tan \gamma \cos \psi \cos \phi - \sin \phi)$$
$$\quad + (\Omega^2 / \cos \gamma) \sin \psi \sin \phi \cos \phi] \tag{6}$$

where r is the radial distance from the center of the Earth to the RLV, normalized by the radius of the Earth $R_0 = 6378$ km. The longitude and latitude are θ and ϕ, respectively. The Earth-relative velocity V is normalized by $V_c = \sqrt{(g_0 R_0)}$ with $g_0 = 9.81$ m/s². The terms D and L are the aerodynamic drag and lift accelerations in g, that is, $D = \rho (V_c V)^2 S_{ref} C_D / (2 m g_0)$ and $L = \rho (V_c V)^2 S_{ref} C_L / (2 m g_0)$, where ρ is the atmospheric density, S_{ref} the reference area of the RLV, and m the mass of the RLV. Note that D and L are also functions of α, the angle of attack, through the dependence of the drag and lift coefficients C_D and C_L on α. The flight-path angle of the Earth-relative velocity is γ and σ the bank angle. The velocity azimuth angle ψ is measured from the North in a clockwise direction. The differentiation is with respect to the dimensionless time $\tau = t/\sqrt{(R_0/g_0)}$. Finally, Ω is the Earth self-rotation rate normalized by $\sqrt{(g_0/R_0)}$. Note that the effects of the Earth self-rotation on V and γ dynamics are not small compared to other terms at the entry of the atmosphere and, thus, should not be ignored in 3DOF entry trajectory planning as is usually done in trajectory tracking law design.

B. Entry Trajectory Constraints

Typical inequality entry trajectory constraints include

$$\dot{Q} \leq \dot{Q}_{max} \tag{7}$$

$$|L \cos \alpha + D \sin \alpha| \leq n_{z_{max}} \tag{8}$$

$$q \leq q_{max} \tag{9}$$

$$(1/r - V^2)(1/r) - L \cos \sigma_{EQ} \leq 0 \tag{10}$$

where Eq. (7) is a constraint on the heating rate at a specified point on the surface of the RLV, with $\dot{Q} = k \sqrt{\rho} V^{3.15}$ for a constant k. Usually, there will be a number of such heat rate constraints imposed on strategic points on the RLV. Although, for simplicity, only one heat rate constraint is used in this paper, the methodology has no inherent difficulty in handling multiple heat rate constraints. As we shall see later, the constraint (7) only needs to be replaced by the envelope of all of the heat rate constraints in the presence of multiple heat rate constraints. Similarly, if the heat rate constraints are replaced by body temperature limits, such as the case for the shuttle,[1] the envelope of all of the temperature limits in the velocity–altitude space is all that is needed. The constraint Eq. (8) is on the aerodynamic load (in gravity g) in the body-normal direction. Depending on the vehicle configuration and mission, this constraint may be replaced by the total load constraint:

$$\sqrt{L^2 + D^2} \leq n_{max} \tag{11}$$

Constraint Eq. (9) is on the dynamic pressure with $q = \rho (V_c V)^2 / 2$. The parameters $\dot{Q}_{max}$, $n_{z_{max}}$ (n_{max}), and q_{max} are vehicle-dependent constants. These constraints are "hard" constraints, meaning that they should be enforced strictly. When held in equality, the last constraint Eq. (10) is called the equilibrium glide condition (EGC) at $\sigma = \sigma_{EQ}$, where σ_{EQ} is a specified constant. The EGC is obtained by omitting the Earth self-rotation terms and setting $\dot{\gamma} = 0$ and $\gamma = 0$ in Eq. (5). This constraint serves to reduce the phugoid oscillations in altitudes along the entry trajectory and to preserve the bank angle margin so that $\sigma \geq \sigma_{EQ}$ during most of the flight. The latter allows sufficient trajectory control to account for dispersions. The constraint (10) is a soft constraint in the sense that its observance need not be absolutely strict, particularly in the final portion of the entry trajectory.

The entry trajectory terminates at some distance from the landing site where the guidance is handed over to the terminal area energy management (TAEM) guidance system. At the TAEM interface, the entry trajectory must have the correct conditions to ensure that successful TAEM and approach/landing flight is possible. These conditions form the terminal conditions for the entry trajectory in terms of

$$r_f = r_{TAEM}, \qquad V_f = V_{TAEM}, \qquad s_f = s_{TAEM} \tag{12}$$

where s_f is the value of range to go s_{togo}, defined to be the range from the RLV to the tangency of the heading alignment cone (HAC) near an end of the runway. The coordinates of the center of the HAC are known. The TAEM altitude r_{TAEM}, velocity V_{TAEM}, and range to HAC s_{TAEM} are all specified for a given RLV. The flight-path angle at TAEM, on the other hand, may or may not be required to be at a fixed value. In addition, the Earth-relative velocity vector at the TAEM interface should be pointing nearly to the HAC tangency. Let $\Delta \psi_f$ be the difference between the velocity azimuth angle and the line-of-sight angle from the RLV to the HAC at the TAEM interface. This condition is then represented by

$$|\Delta \psi_f| \leq \Delta \psi_{TAEM} \tag{13}$$

This condition stipulates that the final velocity vector should be directed at the HAC within a given tolerance $\Delta \psi_{TAEM}$. Figure 1 shows the geometry of the entry flight.

The bank angle magnitude at the TAEM interface oftentimes is another parameter for which constraints may be desired. Too large a σ_f could result in large transient response for TAEM guidance and
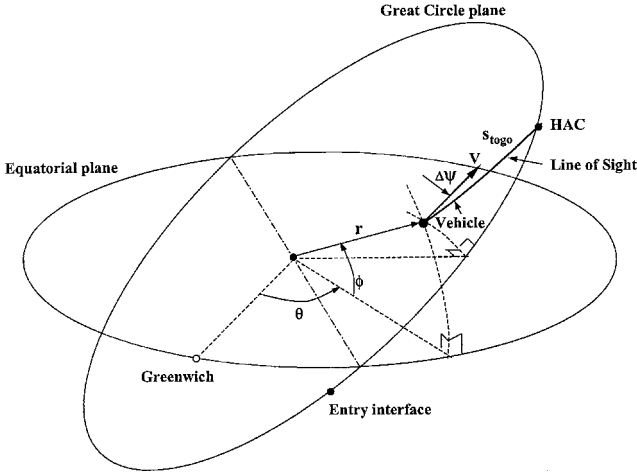
Fig. 1   Geometry of entry flight.

control, and even make recovery unachievable for a less maneuverable RLV. Thus, the constraint

$$|\sigma_f| \leq \sigma_{\text{TAEM}} \tag{14}$$

for a given $\sigma_{\text{TAEM}} > 0$ may also be imposed.

C.   Objective and Assumptions

The entry reference trajectory generation problem is defined as follows: Given the entry conditions, the path constraints, and terminal conditions at the TAEM interface as in the preceding section, find the state history of $\boldsymbol{x} = \{r \ \theta \ \phi \ V \ \gamma \ \psi\}^T$ and the corresponding trajectory control $\boldsymbol{u} = \{\sigma \ \alpha\}^T$ such that the following conditions hold:

1) The state and control profiles $\boldsymbol{x}(t)$ and $\boldsymbol{u}(t)$ satisfy the 3DOF equations of motion, Eqs. (1–6).

2) All of the required TAEM interface conditions are satisfied by $\boldsymbol{x}(t_f)$ and $\boldsymbol{u}(t_f)$.

3) The trajectory observes all of the imposed path constraints.

4) The α profile is consistent with the thermal requirements and vehicle trim capability. Both σ and α profiles do not exceed the flight-control system authority in terms of the maximum magnitudes, rates, and accelerations of σ and α.

A pair $[\boldsymbol{x}(t) \ \boldsymbol{u}(t)]$ that meets the preceding conditions is called a feasible trajectory. The following assumptions establish the scope of applicability of our method:

1) The entry flight is lifting entry, that is, $L/D \neq 0$.

2) All of the trajectory path constraints can be expressed as constraints in the velocity–altitude space for a given α profile.

3) For the given entry conditions, path constraints, TAEM conditions, and vehicle capability, there exists a least one feasible trajectory.

4) A nominal α vs velocity (or Mach number) profile is available, and limited variations about this nominal profile are allowable.

The last assumption is not a necessity for the algorithm, but a practical condition. An arbitrarily designed $\alpha(t)$ profile may not be compatible with the requirements of thermal protection and flight trim conditions. Furthermore, a nominal α profile, once determined for a given vehicle, typically does not change significantly from mission to mission. The assumption 2 encompasses the common path constraints considered in entry flight.

III.   Algorithm

A.   Outline

For trajectory generation purposes, the algorithm tactically divides the entry trajectory into three phases: 1) initial descent phase, 2) quasi-equilibrium glide phase, and 3) pre-TAEM phase. The trajectory in each phase has its own distinctive characteristics. The initial descent is a "controlled fall" that takes the RLV from the entry interface at about 120 km in altitude to an altitude of about 80 km, where the dynamic pressure has reached a sufficient level for aerodynamic lift to become influential in shaping the trajectory.

The quasi-equilibrium glide phase covers the majority of the entry trajectory, where all of the path constraints must be observed and the range achieved must be correct for the RLV to reach the landing site. In the pre-TAEM phase, the flight-path angle, as well as the altitude, decrease rapidly. The trajectory must be such that all of the TAEM conditions are met at the end of this phase.

In the first two steps of trajectory planning, the 3DOF trajectory (longitudinal plus lateral) in the initial descent phase and the longitudinal profiles of the entry trajectory in the pre-TAEM phase are found. Next, close estimates of the longitudinal profiles in the quasi-equilibrium glide phase are determined. At this point, all of the path constraints, range requirements, TAEM velocity, altitude, and flight-path angle conditions are satisfied by the combined longitudinal profiles from the three phases. The associated magnitude of the bank angle is also known. In the final step, Eqs. (1–6) are integrated by use of the bank angle and angle of attack, which are required to track these longitudinal profiles. The sign of the bank angle is determined by selecting the appropriate bank reversal point so that the heading error at the TAEM interface is within tolerance. When this last step is done, a complete 3DOF entry trajectory satisfying the dynamic equations and all of the imposed constraints is found.

In the following, the concept of quasi-equilibrium glide condition and its role in path-constraint enforcement are first described. The details in each of the three phases and the preceding steps are presented thereafter.

B.   Quasi-Equilibrium Glide Condition

At the core of this algorithm for path-constraint enforcement is the use of the quasi-equilibrium glide condition. It is well known in entry flight mechanics that in a major portion of a lifting entry trajectory, the flight-path angle γ is small and varies relatively slowly. Setting $\cos \gamma = 1$ and $\dot{\gamma} = 0$ in Eq. (5) and ignoring Earth rotation gives

$$L \cos \sigma + (V^2 - 1/r)(1/r) = 0 \tag{15}$$

When σ is a constant, this condition is traditionally referred to as the equilibrium glide condition. In actual flight, σ is not necessarily a constant. One can interpret this phenomenon from a different perspective: for a major portion of the lifting entry flight, at any point of the trajectory where the pair $[r(t), V(t)]$ is given, the value of the bank angle at that point will be close to the corresponding value of $\sigma(t)$ satisfying condition (15). Clearly the value of σ from Eq. (15) is generally different from one point to another along the trajectory. Therefore, we shall call condition (15) the quasi-equilibrium glide condition (QEGC) to signify that time-varying σ is admitted in Eq. (15). We shall use Eq. (15) as a general integral of the entry dynamics from an altitude where sufficient dynamic pressure has been built (about 80–85 km) to a cutoff velocity. Below this cutoff velocity, the flight-path angle begins to vary rapidly, and the QEGC is no longer a good representation of the actual motion. A proper choice of the cutoff velocity will be dependent on the lifting capability of the vehicle. For example, for the X-33 and X-38 vehicles, which have relatively low hypersonic maximum L/D ratios of about 0.8 and 1.0, respectively, we find that 1700–2000 m/s is a reasonable range for the cutoff velocity. On the other hand, for the space shuttle, which has higher L/D value, the QEGC still remains sufficiently accurate even at the TAEM interface. Thus, for shuttle-type vehicles, it is possible to use only the initial descent and quasi-equilibrium glide phases. To be applicable to different classes of RLVs, however, the algorithm retains the pre-TAEM phase for all vehicles. The cutoff velocity for QEGC can be set by the user if the user so wishes.

The QEGC provides a simple yet effective means to shape the altitude vs velocity profile by choosing bank angle σ. For a given value of V at a point on the trajectory, if a value of σ is selected, the altitude at this point satisfies the QEGC with sufficient accuracy. If σ is selected between a minimum and a maximum value, the corresponding altitude will be between a maximum and a minimum. This observation and assumption 2 in Sec. II.C lead to an efficient way to enforce the path constraints: Select σ between proper velocity-dependent upper and lower bounds. The corresponding altitude vs velocity profile would then satisfy all of the path constraints. The admissible region specified by the path constraints (7–10) is called the

a)

b)
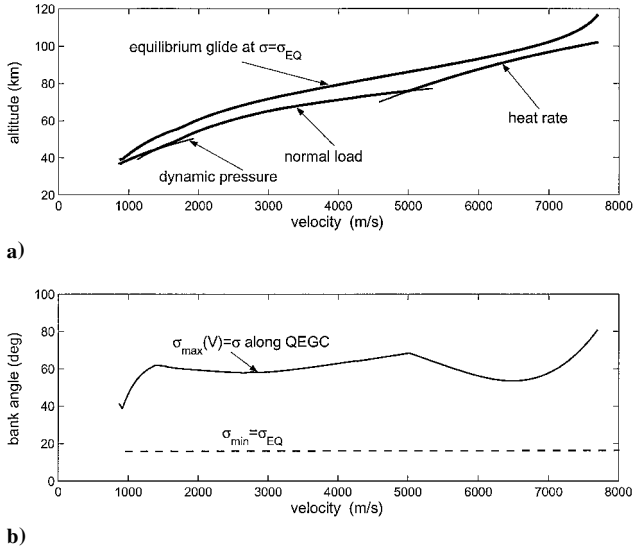
Fig. 2   Entry flight a) corridor boundaries and b) associated QEGC bank angle.

entry flight corridor. The upper boundary of the this corridor in the velocity–altitude space is given by the boundary of the equilibrium glide constraint (10). To enforce the constraint Eq. (10), one obvious bound for σ should be $\sigma_{min} = \sigma_{EQ}$. Let the lower boundary of the entry flight corridor be represented by $l(r, V)$, where $l(r, V)$ clearly is the envelope of the boundaries of constraints (7–9). For a given V, there is a corresponding point on $l(r, V)$, represented by (r, V). A value of σ at this point can be obtained from the QEGC Eq. (15). This value, denoted by $\sigma_{max}(V)$ because it is velocity-dependent, will be the upper bound for σ at this velocity.

Figure 2 shows a flight entry corridor and the corresponding σ_{min} and σ_{max} using the data for the X-33 vehicle. For any V in the range where the QEGC is valid, if the bank angle on the trajectory is limited by

$$\sigma_{EQ}(V) \le \sigma(V) \le \sigma_{max}(V) \qquad (16)$$

then the corresponding trajectory will be inside the entry flight corridor, thus respecting all of the path constraints. In the preceding equation, $\sigma_{EQ}(V)$ is used to bring out that σ_{EQ} can be a velocity-dependent piecewise constant, as it is in some cases. In the case of multiple heat rate constraints, the envelope $l(r, V)$ will be formed by the boundaries of all of the heat rate constraints, instead of just a single one and constraints (8) and (9). The preceding arguments will still be valid. In fact, the same remains true for any other constraints not included in this paper, as long as they meet assumption 2.
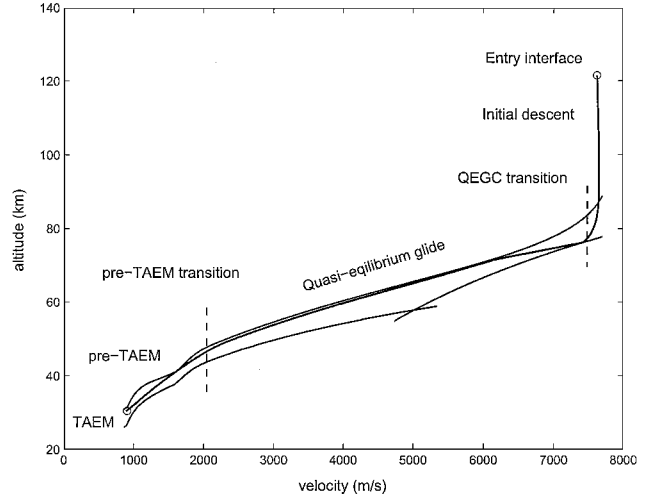
C.   Initial Descent

Above 80–85 km in altitude, the QEGC is not valid because the atmospheric density is too low. The path constraints are not a concern above that altitude for the same reason. Starting at the entry interface, the RLV needs to descend and enter the entry flight corridor, where we want the trajectory to transit smoothly onto a QEGC profile. This transition point marks the end of the initial descent phase. To determine the initial descent trajectory, the nominal α and a constant bank angle $\sigma_{descent}$ are used to integrate the 3DOF equations of motion (1–6) numerically with the given entry conditions. The sign of $\sigma_{descent}$ is such that the aerodynamic lift contributes to reduce the magnitude of $\Delta\psi$, the heading error to the HAC. For a given constant, $\sigma_{descent}$ Eqs. (1–6) are integrated until the following condition is satisfied:

$$\left| \frac{dr}{dV} - \left(\frac{dr}{dV} \right)_{QEGC} \right| < \delta_0 \qquad (17)$$

where $\delta_0 > 0$ is a small preselected value and, from Eqs. (1) and (4) with Ω ignored,

$$\frac{dr}{dV} = \frac{V \sin\gamma}{-D - \sin\gamma/r^2} \qquad (18)$$

Fig. 3   Composition of entry trajectory.

The quantity $(dr/dV)_{QEGC}$ is the slope of the QEGC at the current point $(r \ V)$. It can be obtained by differentiating the QEGC once with respect to V. Once the condition (17) is met, the slopes of the initial descent trajectory and the intersecting quasi-equilibrium glide profile in the velocity–altitude space closely match. A possible transition onto the QEGC is found at this point. Let σ_0 be the corresponding value of bank angle calculated from the QEGC at this point. The choice of $\sigma_{descent}$ is made as follows: When started at zero, the magnitude of $\sigma_{descent}$ is increased by a fixed increment repeatedly. For each $\sigma_{descent}$, the difference of $|\sigma_{descent} - \sigma_0|$ is recorded and compared to the last one. Note that σ_0 also varies as $\sigma_{descent}$ changes. This difference is initially decreasing as $|\sigma_{descent}|$ is increased and then starts to increase. The last value of $\sigma_{descent}$ before the preceding difference begins to increase is selected as the magnitude of the bank angle for the initial descent. Such a choice of $\sigma_{descent}$ minimizes the dynamic transient at the QEGC transition point.

The integrated 3DOF state history x, $\sigma_{descent}$, and α are all stored as a part of the final reference trajectory. The range-to-HAC history s_{togo} for this phase is also calculated from θ and ϕ and stored for later use.

Figure 3 gives the entry trajectory in the velocity–altitude space, including the initial descent with the transition onto the QEGC, plus the other two phases of the trajectory to be described in the following sections.

D.   Quasi-Equilibrium Glide Phase

The algorithm will actually complete the pre-TAEM phase before handling the quasi-equilibrium glide (QEG) phase. However, the QEG phase is discussed first to follow the progression of trajectory phases shown in Fig. 3. In this phase, the QEGC is valid, and the primary objectives in trajectory planning are to ensure observance of the path constraints and satisfaction of range requirements. The initial conditions for this phase are those at the QEGC transition point found in the initial descent. The end conditions for the QEG phase in altitude and velocity, represented by r_1 and V_1, are also determined from the pre-TAEM phase, as will be described in the next section. From the QEGC Eq. (15), the magnitude of bank angle at this point, denoted by σ_1, can be found. The range traveled in the pre-TAEM phase is another output from the pre-TAEM phase algorithm. Given this and the known range coverage in the initial descent phase, the required range-to-go in the QEG phase is defined, which should make up for the total range-to-go from entry interface to the HAC. The differential equation for the range-to-go s_{togo} is

$$\dot{s}_{togo} = -(V \cos\gamma \cos\Delta\psi)/r \qquad (19)$$

where $\Delta\psi$ again is the offset angle between the velocity azimuth and the angle of the line of sight to the HAC point, as shown in Fig. 1. By dividing the $\dot{V}$ equation with $\dot{s}_{togo}$ and ignoring Earth rotation,

we get the differential equation for V with s_{togo} as the independent variable:

$$\frac{dV}{ds_{togo}} = \frac{-1}{\cos\gamma\cos\Delta\psi}\frac{r}{V}\left(-D - \frac{\sin\gamma}{r^2}\right) \qquad (20)$$

Note that the independent variable s_{togo} is decreasing. The usual approximation is that $\cos\Delta\psi \approx 1$, that is, the trajectory is assumed to lie nearly inside a great circle plane containing the HAC. We find it beneficial to retain the effect of $\cos\Delta\psi$, particularly for missions with large crossranges. Let $\Delta\psi_0$ be the known value of $\Delta\psi$ at the beginning of the QEG phase, already obtained from the end conditions of the initial descent phase. Let $\Delta\psi_1$ be the estimate of $\Delta\psi$ at the end of the QEG phase, which is obtained in the pre-TAEM phase (cf., the discussion at the end of Sec. III.D). Then the history of $\Delta\psi$ is approximated by

$$\Delta\psi(V) = \Delta\psi_0 + [(V - V_0)/(V_1 - V_0)](\Delta\psi_1 - \Delta\psi_0) \qquad (21)$$

where V_0 is the value of velocity at the beginning of the QEG phase. Because $\gamma \approx 0$ when the QEGC is valid, Eq. (20) can be further simplified:

$$\frac{dV}{ds_{togo}} = \frac{rD}{V\cos\Delta\psi(V)} \qquad (22)$$

Replacing D with $L(C_D/C_L)$ and substituting L from the QEGC, we get

$$\frac{dV}{ds_{togo}} = \left(\frac{1}{r} - V^2\right)\frac{(C_D/C_L)}{V\cos\Delta\psi(V)\cos\sigma} \qquad (23)$$

Note that $r \approx 1$ in dimensionless form. The most influential factor in the preceding equation is $\cos\sigma$ in the QEG phase. If σ is scheduled as a function of V, r can be found from the QEGC for each V. The angle of attack α is known for a given V (assumption 4 in Sec. II.C), as are C_L and C_D from the aerodynamic model. Hence, the right-hand side of Eq. (23) is completely determined. Thus, for any such profile $\sigma(V)$, Eq. (23) can be numerically integrated in the already determined interval of range-to-go to obtain $V(s_{togo})$ as well as $r(s_{togo})$.

Now, the $\sigma[V(s_{togo})]$ profile must be found to 1) observe the path constraints and 2) satisfy the altitude and velocity conditions r_1 and V_1 at the end of the QEG phase. Note that the value of $\sigma(V)$ at the beginning the QEG phase, denoted by σ_0, is already determined from the QEG transition point. Also, the end value of $\sigma(V)$ should be σ_1 from the QEGC. At a midpoint of the QEG phase, define a to-be-determined value σ_{mid}. Then, the triplet $\{\sigma_0 \; \sigma_{mid} \; \sigma_1\}$ can be used to define a two-segment piecewise linear profile $\sigma(V)$. To observe the path constraints, σ will be limited by condition (16):

$$\sigma = \begin{cases} \sigma_{EQ}(V), & \text{if} \quad \sigma(V) < \sigma_{EQ}(V) \\ \sigma(V), & \text{if} \quad \sigma_{EQ}(V) \leq \sigma(V) \leq \sigma_{max}(V) \\ \sigma_{max}(V), & \text{if} \quad \sigma(V) > \sigma_{max}(V) \end{cases} \qquad (24)$$

Figure 4 shows the preceding process with a case where σ is limited in part by $\sigma_{max}(V)$. The resulting σ profile will ensure that no path constraints are violated. In the portion of the trajectory where $\sigma = \sigma_{max}(V)$, the trajectory will ride on the boundaries of the entry flight corridor, as depicted in Fig. 5.

The value of σ_{mid} is determined to force the velocity at the end of the QEG phase, obtained by integration, equal to V_1. When this condition is met, the end value of r from the QEGC will automatically be equal to r_1 because the end value of σ is σ_1, which is obtained from the QEGC using r_1 and V_1. It is evident from Eq. (23) that the lager the magnitude of σ is, the faster the velocity will decrease [noting that $(1/r - V^2) > 0$ and s_{togo} is decreasing], and vice versa. This observation suggests that the end velocity in the QEG phase is a strong monotonic function of σ_{mid}. The secant method is perhaps the simplest yet very effective way to search for σ_{mid},

$$\sigma_{mid}^{(i+1)} = \sigma_{mid}^{(i)} - \frac{\sigma_{mid}^{(i)} - \sigma_{mid}^{(i-1)}}{V_{QEG1}^{(i)} - V_{QEG1}^{(i-1)}}\left(V_{QEG1}^{(i)} - V_1\right) \qquad (25)$$
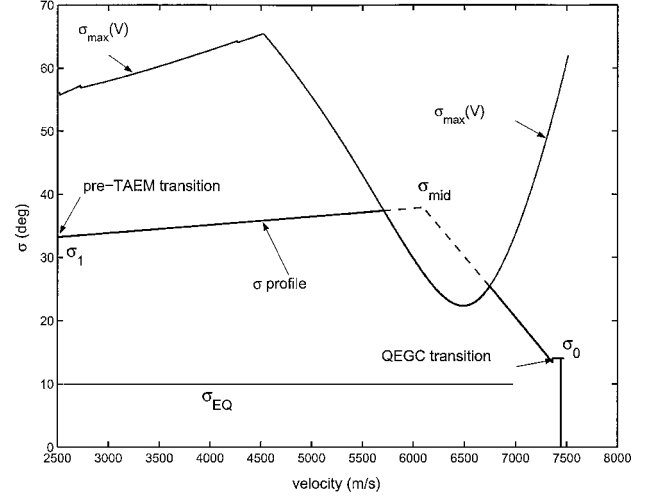

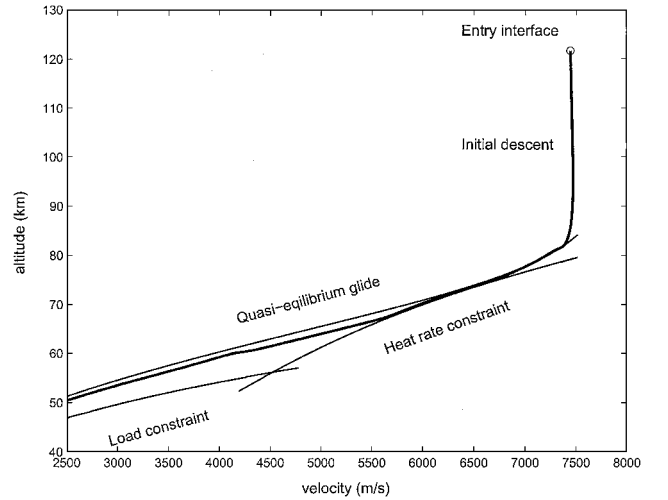
Fig. 4   Possible bank angle profile in the QEG phase.

Fig. 5   Trajectory in velocity-altitude space in QEG phase.

where $V_{QEG1}^{(i)}$ is the end velocity in the QEG phase when $\sigma_{mid}^{(i)}$ is used for σ_{mid}. Note that each evaluation of $V_{QEG1}^{(i)}$ involves numerical integration of Eq. (23). This iteration is highly convergent due to the monotonic functional dependence of V_{QEG1} on σ_{mid}.

Finally, the flight-path angle profile γ in the QEG phase is obtained by numerical differentiation along the QEG profile and stored. At each s_{togo}, we have

$$\gamma(s_{togo}) = \tan^{-1}\left[\frac{r(s_{togo} - \delta s_{togo}) - r(s_{togo})}{\delta s_{togo}}\right] \qquad (26)$$

where δs_{togo} is the range-to-go step size used in the integration. Thus, the longitudinal profiles of the trajectory in the QEG phase, r, V, γ, s_{togo}, and σ (and α as given), are obtained and stored.

E.   Pre-TAEM Phase

A preselected velocity V_1 marks the beginning of the pre-TAEM phase (also the end of the QEG phase). In this phase, the flight-path angle begins to decrease rapidly. The QEGC is no longer a close approximation to the RLV trajectory. If the trajectory planning in the preceding section extends to this phase, the obtained state profiles may not be quite flyable. To avoid iterations and enhance reliability, the algorithm uses a geometric altitude vs velocity curve as an "estimated" trajectory in this phase. Then the actual trajectory satisfying the 3DOF dynamic equations is obtained by numerically integrating equations of motion backward from the TAEM interface to a pre-TAEM point with the bank angle required to track the geometric altitude–velocity curve. Specifically, a fourth-order polynomial

$$r_d = a_4 V^4 + a_3 V^3 + a_2 V^2 + a_1 V + a_0 \qquad (27)$$

is used to define the estimated history for the altitude as a function of the velocity. To determine the five coefficients a_i, a value of r_1 is chosen to be the altitude at V_1, the cutoff velocity for the QEG phase. The choice of r_1 may be the middle point of the entry flight corridor at $V = V_1$. The point (V_1, r_1) will be the endpoint of the QEG phase. Thus, the slope of $(\mathrm{d}r/\mathrm{d}V)$ at this point is specified by the QEGC. At the other end, the TAEM interface altitude and velocity are prescribed in Eq. (12). Two other parameters are chosen at the TAEM interface: the flight-path angle γ_f, if not already specified by the mission requirements, and the TAEM bank angle σ_f. The choice of γ_f where $\gamma_f < 0$ can be made in a range and is not critical to the algorithm. Any choice of σ_f that satisfies Eq. (14) is acceptable. With r_f and V_f, γ_f, and σ_f specified, the slope $\mathrm{d}r/\mathrm{d}V$ and curvature $\mathrm{d}r^2/\mathrm{d}^2V$ are well defined at the TAEM interface because

$$\frac{\mathrm{d}r^2}{\mathrm{d}^2V} = G_r \cos\sigma + H_r \tag{28}$$

where

$$G_r = \frac{L}{\dot{V}^2}\cos\gamma\left(1 + \frac{\sin\gamma}{r^2\dot{V}}\right) \tag{29}$$

$$H_r = \frac{\sin\gamma}{\dot{V}} + \frac{D_V\dot{r}}{\dot{V}^2} - \frac{2\dot{r}^2\sin\gamma}{r^3\dot{V}^3}$$
$$+ \frac{1}{r\dot{V}^2}\cos\gamma^2\left(1 + \frac{\sin\gamma}{r^2\dot{V}}\right)\left(V^2 - \frac{1}{r}\right) \tag{30}$$

In the preceding equation, $D_V = \partial D/\partial V$. The value of $\mathrm{d}^2r/\mathrm{d}V^2$ based on the choice of σ_f ensures that the geometric curve (27) is flyable at least near the TAEM interface. By now we already have five known conditions [three at V_f for $r = r_f$, $(\mathrm{d}r/\mathrm{d}V)_f$, and $(\mathrm{d}r^2/\mathrm{d}^2V)_f$ and two at V_1 for $r = r_1$ and $(\mathrm{d}r/\mathrm{d}V)_1$]. The coefficients in Eq. (27) can be uniquely determined.

The σ profile needed to fly trajectory (27) is found by actually tracking the curve $r_d(V)$. A linear time-varying feedback control law with the gains determined by a linear quadratic regulator approach is used for this purpose. Further description on the merits of such a control law will be given in the next section. The reference bank angle needed for the linearization is obtained by differentiating Eq. (27) twice and using the equations of motion.

The actual state trajectory is then generated by integrating the 3DOF Eqs. (1–6) backward from the TAEM interface with σ found by tracking Eq. (27). Some of the initial conditions for the backward integration are already specified, such as $r_f = r_{\mathrm{TAEM}}$, $V_f = V_{\mathrm{TAEM}}$, and γ_f. The missing initial conditions for θ, ϕ, and ψ are determined as follows: Along the line of sight (LOS) of the great circle from the entry point to the HAC, determine the point where the range to HAC is equal to the required value given in Eq. (12). The coordinates (θ and ϕ) at this point are used as the initial conditions for θ and ϕ in the backward integration; the initial value of ψ is taken to be the LOS azimuth angle at this point so that $\Delta\psi_f = 0$ at the TAEM interface. These approximations do not appear to cause a noticeable discrepancy in the final trajectory when the integrated lateral state variables in this phase are used to estimate the range-to-go history. This is because in the relatively short distance of the pre-TAEM phase, the range-to-go variation is nearly independent of the actual velocity azimuth and the coordinates of the beginning of the pre-TAEM phase. As long as $\Delta\psi = 0$, the range to HAC is the same at the end of this phase (as in the case of planar motion).

There are no iterations involved in this phase. The backward integration is terminated at $V = V_1$. The longitudinal state profiles r, V, γ, s_{togo}, plus σ are now obtained and stored. The r vs V history will be close to the one in Eq. (27). Note that even if the value of r at V_1 is not exactly r_1 as stipulated by Eq. (27), we can simply redesignate the actual value of r at this point as r_1 (recall that r_1 was arbitrarily chosen). The newly designated point (V_1, r_1) will be the endpoint of the QEG phase. The TAEM conditions on r_f, V_f, γ_f, and σ_f, however, are always met because these are the initial conditions for the backward integration. The longitudinal profiles are all flyable because they satisfy the equations of motion. Another outcome of the backward integration is the value of $\Delta\psi_1$ at the beginning of the pre-TAEM phase. This value is largely determined by the bank

angle required to track the geometric curve (27), again practically invariant regardless of the actual direction of the trajectory when the vehicle enters the pre-TAEM phase. This value of $\Delta\psi_1$ is used in the QEG phase for approximating the profile $\Delta\psi(V)$ in Eq. (21).

F. Search for Bank Angle Reversal Point: Completion of the 3DOF Trajectory

After the preceding three parts of the algorithm are completed, the longitudinal profiles are obtained for the entire entry trajectory, but not the correct lateral profiles (except for the initial descent phase where the full 3DOF trajectory is already established). We schedule the longitudinal profiles with respect to the range-to-go, represented by $r^*(s_{\mathrm{togo}})$, $V^*(s_{\mathrm{togo}})$, and $\gamma^*(s_{\mathrm{togo}})$. Similarly, the magnitude of the associated $|\sigma^*(s_{\mathrm{togo}})|$ and $\alpha^*(s_{\mathrm{togo}})$ are known too. The entire 3DOF trajectory is completed by integrating Eqs. (1–6) from the QEG transition point to the TAEM interface with $|\sigma|$ and α required to track $r^*(s_{\mathrm{togo}})$ and $V^*(s_{\mathrm{togo}})$. Note that, by the way in which $r^*(s_{\mathrm{togo}})$ and $V^*(s_{\mathrm{togo}})$ are obtained, all of the path constraints (7–10), and the TAEM conditions (12) and (14) will be satisfied if $r^*(s_{\mathrm{togo}})$ and $V^*(s_{\mathrm{togo}})$ are tracked closely. Because the sign of σ does not impact the longitudinal dynamics [Eqs. (1), (4), and (5)], it does not affect the tracking of $r^*(s_{\mathrm{togo}})$ and $V^*(s_{\mathrm{togo}})$. However, the vehicle heading angle ψ is dependent on the sign of σ. The sign of σ is determined by the bank angle reversal logic, to be described later in this section, so that the heading error to HAC at the TAEM interface is within the specified range as required in Eq. (13).

The tracking control laws used are linear time-varying feedback control laws

$$\delta\boldsymbol{u} = -K(s_{\mathrm{togo}})\delta\boldsymbol{x}_{\mathrm{lon}} \tag{31}$$

where $\delta\boldsymbol{u} = (\delta\sigma\ \ \delta\alpha)^T$ and $\delta\boldsymbol{x}_{\mathrm{lon}} = (r\ \ V\ \ \gamma)^T - (r^*\ \ V^*\ \ \gamma^*)^T$. The gain K is obtained offline with the linear quadratic regulator (LQR) approach at different points along a nominal trajectory and scheduled online with respect to range-to-go. Dukeman has demonstrated very good performance of such an LQR tracker.[10] More importantly for our applications, he shows that for tracking the longitudinal profiles, the LQR gains need not be recomputed for different reference entry trajectories for the same vehicle. This means that one set of gains will work well for the same vehicle for different reference trajectories and, thus, will be applicable for onboard trajectory generation.

The magnitudes of σ and α required by the vehicle dynamics to fly the obtained longitudinal profiles are then given by

$$|\sigma| = |\sigma^* + \delta\sigma| \tag{32}$$

$$\alpha = \alpha^* + \delta\alpha \tag{33}$$

Note that the magnitude of $\delta\boldsymbol{u}$, although usually small, will not be zero because in the QEG portion the references $\boldsymbol{x}_{\mathrm{lon}}^*$ and σ^* are obtained using the QEGC, an approximation to the longitudinal dynamics in a strict sense.

The sign of the initial bank angle is chosen to help reduce the heading error to HAC $\Delta\psi$, beginning from $\sigma_{\mathrm{descent}}$ in the initial descent. The sign of the bank angle is reversed at a range s_{rev} to the HAC. The appropriate s_{rev} is sought so that when the RLV reaches the prescribed distance s_{TAEM} to the HAC, the magnitude of $\Delta\psi$ is within the tolerance specified in Eq. (13). This search is performed iteratively. A metric of "miss distance," denoted by s_g, is established for measuring how close a trajectory is to the correct heading condition at the TAEM interface. Figure 6 demonstrates the geometry and definition of s_g. The circle centered at the HAC has the radius of s_{TAEM} and represents the TAEM interface. In case 1, the bank reversal takes place too late. When the RLV reaches the interface, the "projected crossing point" is defined by extending a straight line along the velocity azimuth to intersect with the LOS from the bank reversal point to the HAC. The value $s_g > 0$ is the distance between the HAC and the projected crossing point. In case 2, the bank reversal happens too early. The trajectory crosses the LOS from the bank reversal point to the HAC before reaching the TAEM interface. In this case, $s_g < 0$ is (the negative of) the distance between the crossing point and the HAC. Clearly, the desired value is $s_g = 0$, which is the case when the RLV is at the TAEM interface with the
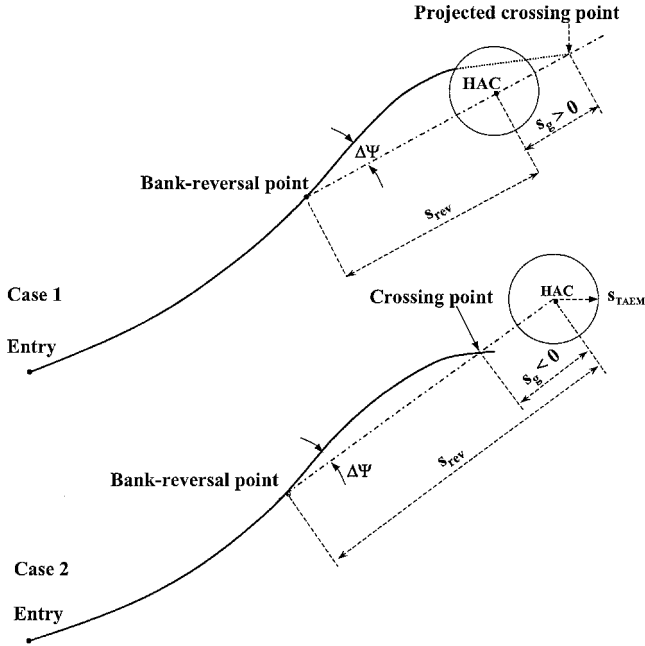
Fig. 6 Geometry for determining bank reversal point.

Fig. 7 Flowchart of the algorithm.

heading angle pointing directly to the HAC. The metric s_g is obviously monotonic, at least in a range, with respect to the parameter s_{rev}. The secant method proves again to be effective in finding the correct s_{rev},

$$s_{rev}^{(i+1)} = s_{rev}^{(i)} - \left[s_g^{(i)} \Big/ \left(s_g^{(i)} - s_g^{(i-1)} \right) \right] \left(s_{rev}^{(i)} - s_{rev}^{(i-1)} \right) \qquad (34)$$

For each $s_{rev}^{(i)}$, the sign of σ is determined by the bank reversal logic. The system equations (1–6) are numerically integrated until the TAEM interface is reached (case 1 in Fig. 6), or at a point when the ground track is no longer moving toward the HAC before reaching the TAEM interface (case 2 in Fig. 6). The value of $s_g^{(i)}$ is calculated for updating the next $s_{rev}^{(i+1)}$ if necessary. Note that by tracking the longitudinal profiles with range-to-go as the independent variable, the range and other TAEM conditions remain to be satisfied in the process.

The preceding iteration requires two starting guesses, $s_{rev}^{(0)}$ and $s_{rev}^{(1)}$. In Ref. 11 a scheme is developed to generate educated guesses for $s_{rev}^{(0)}$ and $s_{rev}^{(1)}$ based on the information already obtained in the pre-TAEM phase planning. With such a scheme, the process is completely automated, with no need for user supplied guesses. Once this last iteration process converges, a complete feasible 3DOF trajectory in the state space is generated and ready to serve as the reference of the entry flight.

In most cases a single bank reversal suffices. If more than one bank reversal is desired for the purpose of shaping the ground track, the algorithm allows more bank reversals based on the heading error $\Delta \psi$. Just like the shuttle, whenever $|\Delta \psi|$ exceeds a preset threshold value Δ_ψ, the sign of σ is reversed. The last bank reversal, however, will always be determined by the aforementioned algorithm at an s_{rev}. There would be just a single bank reversal along the 3DOF trajectory found by the algorithm if Δ_ψ is set to be very large (so that the threshold value would never be surpassed). Otherwise, more than one bank reversal may be present along the trajectory.

It is in the process described in this section that the control authority constraints in terms of maximum magnitude, rate, and acceleration limits in σ and α may be enforced.

As a summary of the various parts of the algorithm, Fig. 7 is a flowchart that captures the main blocks of the algorithm.

Once the reference trajectory is generated, the entry guidance commands will be determined by feedback control laws that track the reference trajectory. To be compatible with the onboard trajectory-planning capability, the control law should not require any offline gains generation and tuning for tracking 3DOF (longitudinal and lateral) reference profiles. Likewise, it should ensure closed-loop stability for any possible trajectories. A control law with
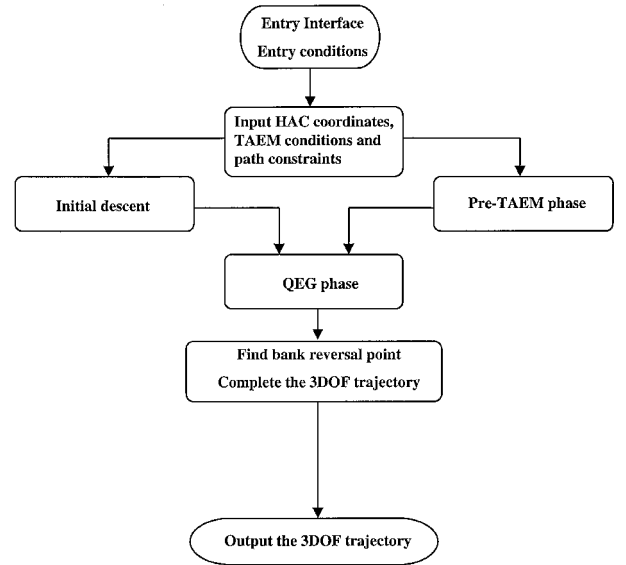
these characteristics is the linear time-varying receding-horizon control law recently developed.[12] Its application in entry guidance has already been demonstrated.[13]

IV. Testing

The test cases presented in this paper use the models of the X-33 vehicle and the shuttle. More tests for the X-33 and test cases using the X-38 CRV vehicle and mission data can be found in Ref. 11. Apart from being considerably smaller, the X-33 model represents a vehicle that has 40% lower hypersonic lift-to-drag ratio than that of the shuttle. Successful applications of the proposed trajectory planning algorithm to these two very different vehicles should provide evidence of strong cross-cutting applicability of the algorithm. In the following simulations, the 3DOF reference trajectory is generated only once at the beginning of the entry flight. However, the algorithm can certainly be used repeatedly during the entry flight if necessary. The possible reasons for such a need include significant off-nominal dispersions, system or control effector failure, or abort to an alternate landing site. In these scenarios the algorithm would generate a new reference trajectory onboard based on the current conditions and vehicle health information, which would provide great adaptive capability to the entry guidance system.

A. X-33 Vehicle and Missions

The X-33 is a half-scale technology demonstrator for a single-stage RLV. The vehicle has a lifting-body configuration. The vehicle dry weight is about 38,000 kg. Although the X-33 was a suborbital vehicle, mission scenarios for entry from different orbits have been set up at NASA Marshall Space Flight Center (MSFC) for testing advanced guidance and control algorithms.[14] All of the orbital entry missions land at the NASA Kennedy Space Center (KSC). In all of the tests presented here, the X-33 vehicle model and the runway coordinates of the shuttle landing facility at KSC are used. The nine missions developed at MSFC are labeled AGC13–AGC21. The tests performed here are based on these mission specifications with some slight modifications for uniformity. In particular, the following nominal α profile is used for all nine missions:

$$\alpha = \begin{cases} 45 \text{ deg} & \text{if} \quad \text{Mach} \geq 10 \\ 45 - 0.612 \, (\text{Mach} - 10)^2 \text{ deg} & \text{if} \quad 2.5 \leq \text{Mach} < 10 \end{cases} \qquad (35)$$

In addition, the following TAEM conditions are imposed for all nine missions:

1) The TAEM altitude is 30.48 km (100,000 ft).
2) The range to HAC at TAEM interface is 55.56 km (30 n mile).
3) The TAEM velocity is 908.15 m/s (2979.5 ft/s).
4) The TAEM magnitude of the heading error with respect to the HAC is less than 5 deg.

Table 1   X-33 entry missions

Case	Inclination, deg	Downrange, km	Crossrange, km	Heat rate limit, W/m^2
AGC13	51.6	6519	59	794,425
AGC14	51.6	6554	809	794,425
AGC15	51.6	6589	−848	794,425
AGC16	51.6	8160	148	680,935
AGC17	51.6	8715	883	680,935
AGC18	51.6	8197	−778	680,935
AGC19	28.5	7360	267	680,935
AGC20	28.5	7382	752	680,935
AGC21	28.5	7625	380	680,935

5) The magnitude of the TAEM bank angle is less than 30 deg. The vehicle flight control authority is restricted by the following limits:

1) The excursions of α from the nominal profile are no greater than 5 deg.

2) The maximum rates are $|\dot{\alpha}|_{\max} = 5.0$ deg/s and $|\dot{\sigma}|_{\max} = 5.0$ deg/s.

3) The maximum accelerations are $|\ddot{\alpha}|_{\max} = 2.0$ deg/s^2 and $|\ddot{\sigma}|_{\max} = 3.5$ deg/s^2.

The path constraints on the entry trajectories are as follows:

1) The peak heat rate constraint is 794,425 W/m^2 (70 Btu/ft^2 · s) for AGC13–15 and 680,935 W/m^2 (60 Btu/ft^2 · s) for AGC16–21.

2) The peak normal acceleration constraint is 2.5g.

3) The peak dynamic pressure constraint is 14,364 N/m^2 (300 psf).

No equilibrium glide constraint was specified in the MSFC mission requirements. However, we did impose an equilibrium glide constraint of $\sigma_{EQ} = 10$ deg for trajectory shaping purposes.

The nine missions are for entry flights from the International Space Station (ISS) orbit at 51.6-deg inclination (AGC13–18) and from orbit at 28.5-deg inclinations (AGC19–21). These missions are further differentiated by low, high left, and high right cross ranges with a different set of entry conditions for each mission. For the same orbit, the differences in entry conditions result from different deorbit points in orbit. Table 1 lists the orbital inclination, downrange, cross range and peak heat rate limit for each mission. Negative values for cross ranges indicate left cross ranges.

B.   X-33 Nominal Entry Flight

The algorithm described in Sec. III was implemented in the programming language C. The trajectory simulations were performed by using a high-fidelity simulation software developed at MSFC, called MAVERIC. The code for the trajectory generation algorithm was incorporated into the MAVERIC. The reference 3DOF trajectory for each of the nine missions was generated online and stored the first time when entry guidance was called on. After that, this reference trajectory was tracked by a linear time-varying feedback control law.[13] This tracking guidance law provided the bank angle and angle-of-attack commands to MAVERIC for 3DOF simulations. The atmospheric properties were modeled by the Global Reference Atmospheric Model (GRAM),[15] and GRAM mean winds were also included in the simulations. No mission-dependent adjustments of any algorithm parameters or trajectory tracking control law were made. The only changes were the entry conditions and the peak heat rate limit.

Figure 8 shows the comparison of the reference and the actual (MAVERIC-simulated) velocity–altitude profiles for mission AGC21. By and large, the reference profile was closely tracked. Figures 9 and 10 give the comparison of reference and actual bank angle profiles and reference and actual angle-of-attack profiles, respectively. The flown (by MAVERIC) profiles were very close to the reference ones, confirming the validity of the algorithm and the QEG approximation in particular.

Figure 11 shows the bank angle and angle-of-attack histories for all nine missions from MAVERIC simulations. The number by each curve indicates the mission number. The bank angle variations for AGC15 and 18 are given in a separate plot for clarity. The bank angle at the entry interface was assumed to be zero for all cases. It was evident from Fig. 11 that a single bank angle reversal was
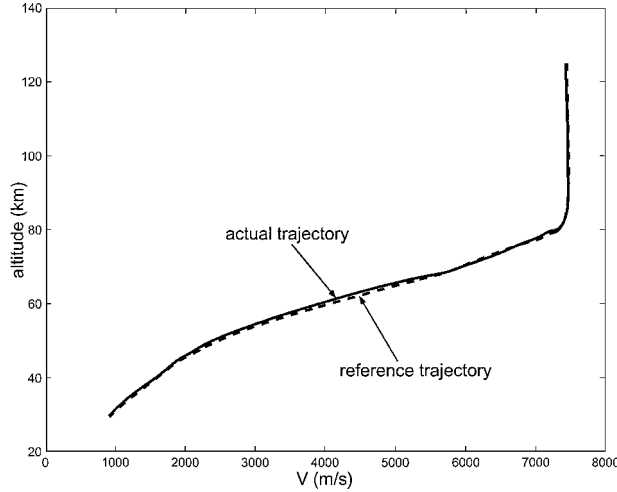

Fig. 8   Comparison of reference and actual X-33 trajectories for mission AGC21.
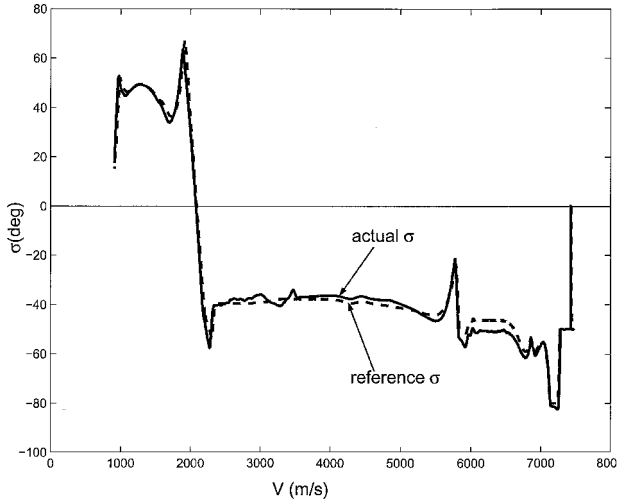

Fig. 9   Comparison of reference and actual bank angles for mission AGC21.

sufficient for all nine missions. Trajectories with two bank reversals are possible, but, for the X-33, the ground tracks would not be much different from those with one bank reversal (Fig. 12) because of the rather limited turning capability of the X33. It can also be seen from Fig. 11 that the final bank angle $|\sigma_f|$ was smaller than 30 deg in all cases. The ground tracks for all of the nine missions are plotted in Fig. 12, which shows the different entry points for the missions.

Figure 13 illustrates the MAVERIC simulated trajectory and the entry flight corridor for mission AGC19. This was a highly constrained case, notably by the low peak heat rate limit. However, the algorithm accurately enforced the heat rate constraint by forcing the reference trajectory to ride on the heat rate boundary for a considerable period, and all was done in about 3 s. The trajectory tracking control law closely tracked the reference so that the actual peak heat rate along the trajectory was 676,963 W/m^2 (59.65 Btu/ft^2 · s), compared to the imposed limit of 680,935 W/m^2 (60 Btu/ft^2 · s). Other path constraints were all within their limits. This was typical of what this algorithm can do in highly constrained cases.

Table 2 lists the TAEM condition errors for all nine cases. The simulations by MAVERIC stopped at the specified TAEM velocity; therefore, no velocity errors were given in Table 2. Note from Table 2 that all of the TAEM conditions were met very accurately from the standpoint of entry guidance. The maximum altitude error $|\Delta r_f|$ was less than 300 m, the maximum range error $|\Delta s_f|$ less than 1.85 km (1 n mile), and the maximum heading error $|\Delta \psi_f|$ less than 5 deg, as required. A single value of $\gamma_f = -7.5$ deg was used for the trajectory design in all of the nine cases.

Finally, the computation times used for generating the 3DOF reference trajectory for each mission are provided in Table 3. Two

Table 2   X-33 TAEM condition errors

Case	Δr_f, m	Δs_f, m	$\Delta \psi_f$, deg	$\Delta \gamma_f$, deg
AGC13	92	−513	2.6	−0.01
AGC14	77	−1787	−3.4	−0.39
AGC15	199	−333	−4.79	0.13
AGC16	110	−156	3.49	−0.91
AGC17	177	−1085	−3.53	−0.48
AGC18	282	370	−3.55	−0.61
AGC19	165	203	2.44	−0.79
AGC20	−74	−339	−3.95	−0.89
AGC21	131	591	4.25	−0.61

Table 3   Computation time

Case	PC, s	UNIX, s
AGC13	2.77	2.18
AGC14	2.56	2.03
AGC15	2.59	2.05
AGC16	3.95	3.13
AGC17	3.54	2.68
AGC18	3.29	2.58
AGC19	2.55	1.99
AGC20	2.53	1.98
AGC21	2.61	2.05

Fig. 10   Comparison of reference and actual angle of attack profiles for mission AGC21.

Fig. 11   X-33 bank angle and angle of attack histories.
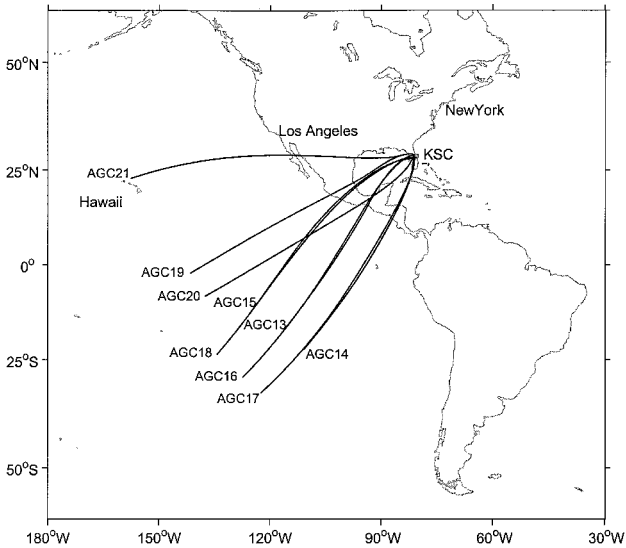
Fig. 12   Ground tracks for all 9 X-33 missions.
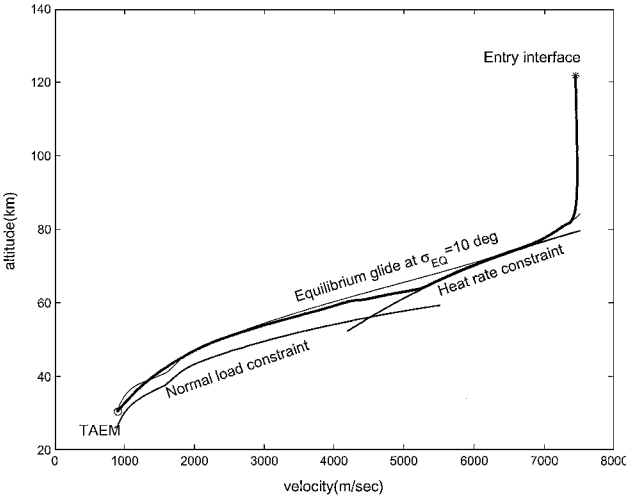
Fig. 13   Entry trajectory for mission AGC19.

values are given in each case. One is for a desktop computer with a 800-MHz processor, and the other is for a UNIX-based workstation with a 500-MHz processor. Note that no effort was made to optimize or streamline the code implementing the algorithm when these computation times were measured. Even so, the time that the algorithm needs for generating a highly constrained 3DOF entry trajectory with flight time of 25 min is only about 2–3 s.

C.   X-33 Dispersion Simulations

To further evaluate the performance of the entry guidance system combining online reference trajectory generation and trajectory tracking with the self-gain-scheduled controller,[13] dispersion studies were done for the preceding missions using Monte Carlo simulations. The uncertainties and modeling errors unknown to the guidance algorithms include those of the GRAM dispersed atmosphere (winds, atmospheric density, etc.), aerodynamic coefficients, navigation data, and mass of the vehicle. These uncertainties were incorporated in the MAVERIC simulations. The entry conditions were not dispersed, but the entry guidance algorithm was called after a 20-s transition period under open-loop guidance from the entry interface on down. Thus, in effect, the initial conditions passed into the entry guidance algorithms were different for each trajectory because of the influence of the aforementioned uncertainties during the transition period. The trajectory planning algorithm generated a reference trajectory each time based on the current initial conditions. This reference trajectory was then tracked by the feedback tracking law, which provided the guidance commands in σ and α.
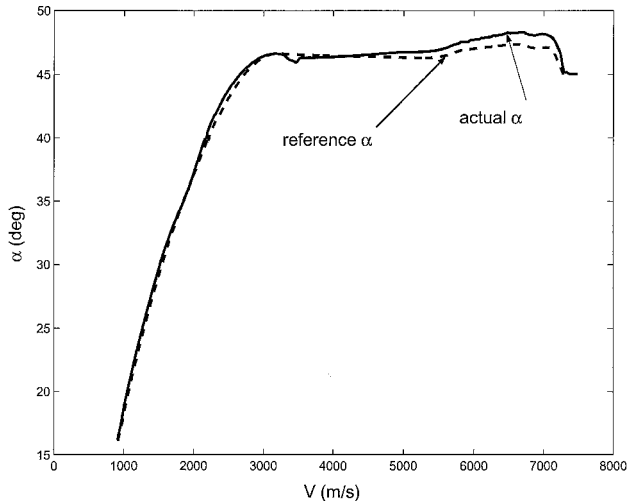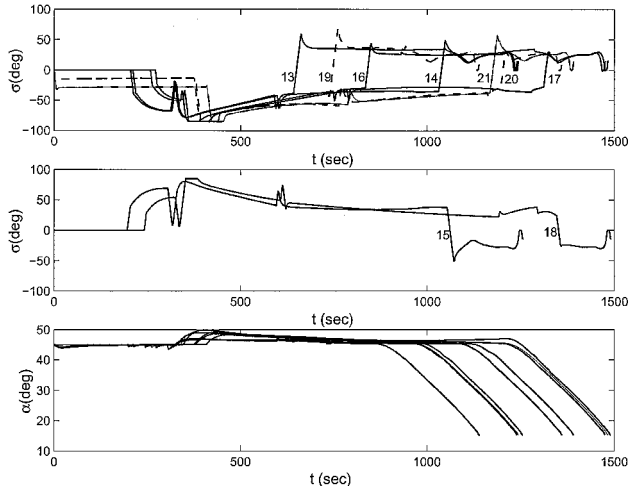
The path constraints, TAEM conditions, and control authority limits were the same as in the nominal flights.

The dispersion simulation results for three missions, AGC13, AGC18, and AGC20 are presented here. They were chosen to represent low, high left, and high right cross range requirements, respectively, and for entry from orbits with different inclinations. A total of 100 trajectories for each mission were simulated. Again, no case-dependent tuning of parameters or algorithm were made.

Figure 14 shows the scatter in the values of the TAEM altitude and velocity from the simulations. The dispersions in altitude were
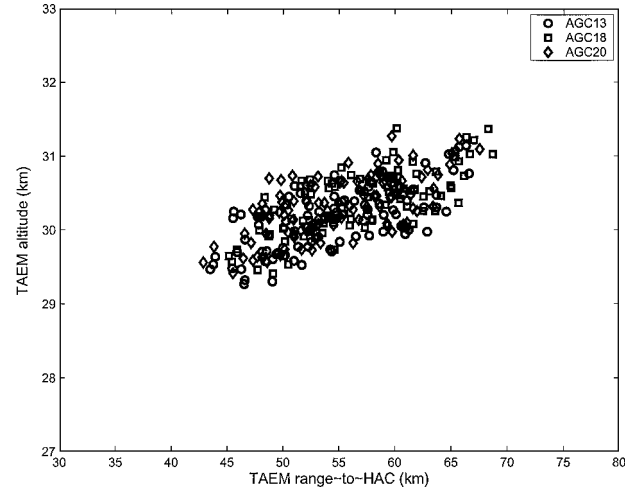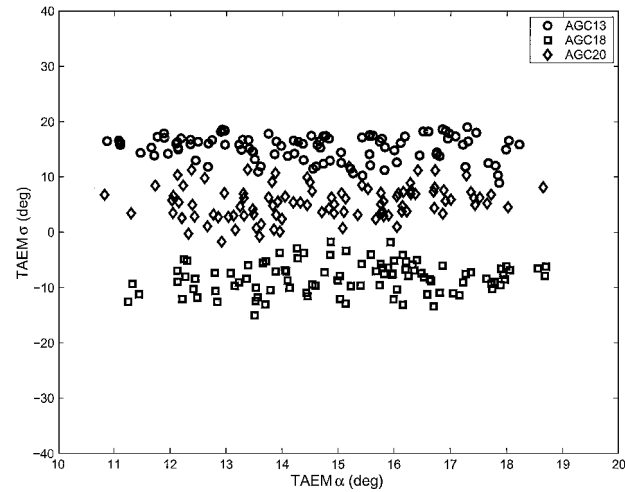

Fig. 14   TAEM altitudes and ranges.

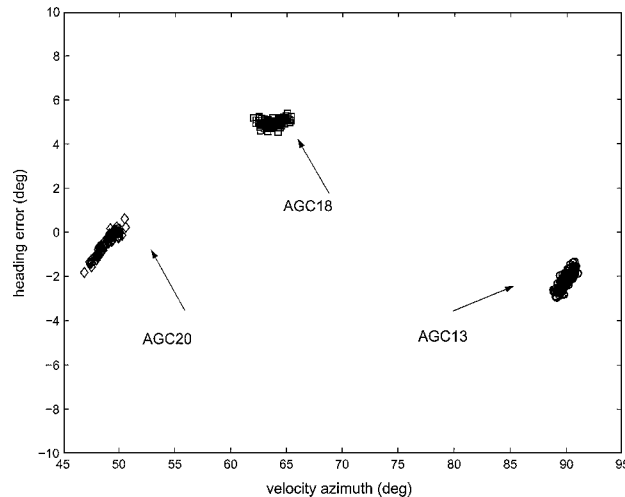**Fig. 15   TAEM bank angles and angles of attack.**

Fig. 16   TAEM heading errors and velocity azimuth angles.

less than 1 km. The range-to-HAC dispersions were within 11 km (6 n mile), which can be accommodated by the TAEM guidance easily. Figure 15 gives the final values of the bank angle and angle of attack. The final bank angle was no greater than 20 deg in magnitude in any case. The final angles of attack were all within ± 5 deg of the nominal TAEM value of 15 deg. The TAEM heading errors with respect to the HAC and the actual heading (velocity azimuth) angles are plotted in Fig. 16. Depending on the mission, the RLV would approach the HAC from a different direction, as reflected by the final heading angles. However, the entry guidance system kept the heading errors all below 5 deg. In the tested cases for the three missions, all trajectories maintained the average peak heat rates within 11,349 W/m^2 (1 Btu/ft$^2 \cdot$ s) of their respective limits, with standard deviations about 18,160 W/m^2 (1.6 Btu/ft$^2 \cdot$ s). The maximum peak heat rates among the trajectories were about 5% over the respective limits, largely due to atmospheric density dispersions.

D.   Space Shuttle Entry Trajectory Planning

The shuttle vehicle data and mission profile were also used in generating entry trajectory with the current algorithm. Specifically, the following TAEM conditions were imposed:

1) The TAEM altitude is 24.384 km (80,000 ft).

2) The range to HAC at the TAEM interface is 92.6 km (50 n mile).

3) The TAEM velocity is 743 m/s.

4) The TAEM magnitude of the heading error with respect to the HAC is less than 5 deg.

5) The magnitude of the TAEM bank angle is less than 30 deg.

The following trajectory control limits are enforced:

1) The excursions of α from the nominal profile is no greater than 5 deg.

2) The maximum rates are $|\dot{\alpha}|_{max} = 5.0$ deg/s and $|\dot{\sigma}|_{max} = 5.0$ deg/s.

3) The maximum accelerations are $|\ddot{\alpha}|_{max} = 1.0$ deg/s^2 and $|\ddot{\sigma}|_{max} = 1.7$ deg/s^2.

The imposed trajectory path constraints are as follows:

1) The peak heat rate constraint is 964,659 W/m^2 (85 Btu/ft$^2 \cdot$ s).

2) The peak total acceleration constraint is 2.5g.

3) The peak dynamic pressure constraint is 16,375 N/m^2 (342 psf).

4) The equilibrium glide constraint at σ_{EQ} is 10 deg.

Note that the shuttle uses temperature limits at various body points instead of peak heat rate for entry trajectory design. We did not have access to the temperature data to formulate the temperature boundary needed in our algorithm. We did have the data for a shuttle entry trajectory, which we call shuttle baseline trajectory hereafter. Based on this trajectory data, we found that the aforementioned peak heat rate constraint appears to address the thermal considerations adequately.

Only trajectory planning was performed. Closed-loop simulations in tracking the reference trajectory were not done at this time.
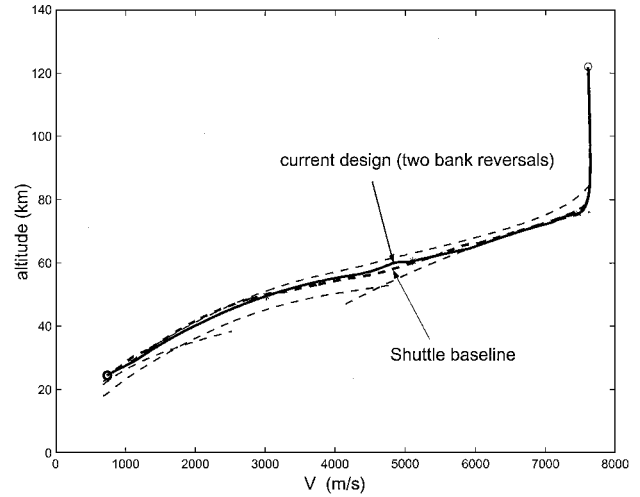

Fig. 17   Comparison of entry trajectory by proposed algorithm and a shuttle baseline trajectory.

Figure 17 shows the entry flight corridor, the trajectory generated by the proposed algorithm, and the shuttle baseline trajectory. To demonstrate that the algorithm allows multiple bank reversals, the bank reversal logic based on heading error was turned on with a threshold limit of 10 deg from entry interface to the range s_{rev}, where the final bank reversal was found by the algorithm to null the heading error at the TAEM interface. This produced a total of two bank reversals, as seen in Fig. 18. If this feature were not activated, a single bank reversal would be found, also plotted in Fig. 18. In contrast, the shuttle baseline trajectory used three bank reversals, as is evident from Fig. 18. The effects of the number of bank reversals are clear from Fig. 19 where the ground tracks are depicted. The ground track of the trajectory with two bank reversals was quite close to that of the shuttle baseline trajectory, whereas the one with a single bank reversal approached the landing site at KSC from a different direction (nearly due west).

The shuttle is a considerably more capable vehicle than the X-33 in terms of flyability. Although not shown here, the algorithm was able to generate easily various entry trajectories with arbitrary perturbations in the conditions at the entry interface so that the cross range and downrange changed for up to 1000 km (in either the plus or minus directions) from the shuttle baseline trajectory. All of these trajectories, including the ones shown earlier, were completed within about the same times as those listed in Table 3.
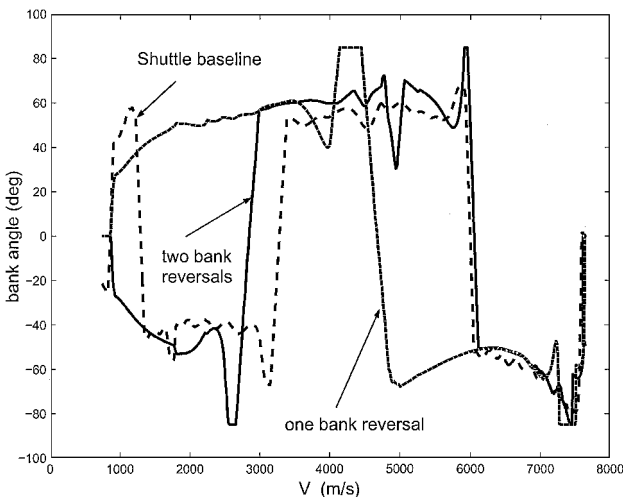

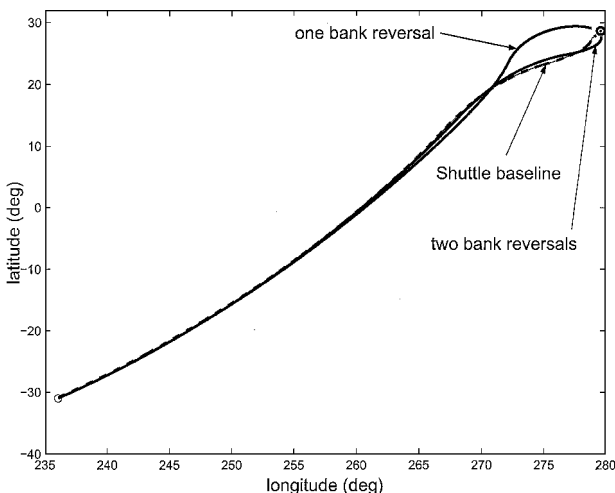**Fig. 18   Comparison of shuttle bank angle profiles.**

Fig. 19   Ground tracks for the shuttle.

V.   Conclusions

A methodology for rapid generation of 3DOF constrained lifting entry trajectories is developed. The ultimate goal is to provide onboard entry trajectory-planning capability. The very high efficiency of the algorithm also makes it an ideal tool for entry mission planning, analysis, and tradeoff studies on the ground. The method is conceptually different from any of the existing approaches for entry trajectory planning. The algorithm can generate a complete flyable 3DOF trajectory subject to stringent path and end-condition constraints within 2–3 s on a desktop computer. High-fidelity simulations in both nominal flight and dispersion studies for a number of mission scenarios using the X-33 model and applications to entry trajectory planning with the shuttle model more than adequately demonstrate the proof of concept of the method. A limitation of the current work lies in suborbital cases for vehicles with low lift-to-drag ratios. For those vehicles, if the entry flight starts at a speed substantially lower than the orbital speed, the quasi-equilibrium glide (QEG) condition may not be valid even at the beginning of the flight. Although a number of components of the algorithm will remain applicable in these cases, modifications to the algorithm related the QEG phase will be needed.

References

[1] Harpold, J. C., and Graves, C. A., "Shuttle Entry Guidance," *The Journal of the Astronautical Sciences*, Vol. 37, No. 3, 1979, pp. 239–268.
[2] Gamble, J. D., Cerimele, C. J., Moore, T. E., and Higgins, J., "Atmospheric Guidance Concepts for an Aeroassisted Experiment," *The Journal of the Astronautical Sciences*, Vol. 36, No. 1–2, 1988, pp. 45–71.
[3] Powell, R. W., "Six-Degree-of-Freedom Guidance and Control-Entry Analysis of the HL-20," *Journal of Spacecraft and Rockets*, Vol. 30, No. 5, 1993, pp. 537–542.
[4] Fuhry, D. P., "Adaptive Atmospheric Reentry Guidance for the Kistler K-1 Orbital Vehicle," *Proceedings of the AIAA Guidance, Navigation, and Control Conference*, Vol. 2, AIAA, Reston, VA, 1999, pp. 1275–1288.
[5] Zimmerman, C., Dukeman, G., and Hanson, J., "An Automated Method to Compute Orbital Entry Re-Entry Trajectories with Heating Constraints," AIAA Paper 2002-4454, Aug. 2002.
[6] Mease, K. D., Chen, D. T., Teufel, P., and Schoenenberger, H., "Reduced-Order Entry Trajectory Planning for Acceleration Guidance," *Journal of Guidance, Control, and Dynamics*, Vol. 25, No. 2, 2002, pp. 257–266.
[7] Roenneke, A. J., "Adaptive Onboard Guidance for Entry Vehicle," *Proceedings of the AIAA Guidance, Navigation, and Control Conference*, AIAA, Reston, VA, 2001.
[8] Girerd, A., and Barton, G., "Next-Generation Entry Guidance: Onboard Trajectory Generation for Unpowered Drop Tests," *Proceedings of the AIAA Guidance, Navigation, and Control Conference*, AIAA, Reston, VA, 2000.
[9] Vinh, N. X., Busemann, A., and Culp, R. D., *Hypersonic and Planetary Entry Flight Mechanics*, Univ. of Michigan Press, Ann Arbor, MI, 1980, pp. 26, 27.
[10] Dukeman, G. A., "Profile-Following Entry Guidance Using Linear Quadratic Regulator Theory," *Proceedings of the AIAA Guidance, Navigation, and Control Conference*, AIAA, Reston, VA, 2002.
[11] Shen, Z., "On-Board Three-Dimensional Constrained Entry Flight Trajectory Generation," Ph.D. Dissertation, Dept. of Aerospace Engineering and Engineering Mechanics, Iowa State Univ., Ames, IA, Aug. 2002.
[12] Lu, P., "Closed-Form Control Laws for Linear Time-Varying Systems," *IEEE Transactions on Automatic Control*, Vol. 45, No. 3, 2000, pp. 537–542.
[13] Lu, P., "Regulation About Time-Varying Trajectories: Precision Entry Guidance Illustrated," *Journal of Guidance, Control, and Dynamics*, Vol. 22, No. 6, 1999, pp. 784–790.
[14] Hanson, J., "Advanced Guidance and Control Project for Reusable Launch Vehicles," AIAA Paper 2000-3958, 2000.
[15] Justus, C. G., and Johnson, D. L., "The NASA/MSFC Global Reference Atmospheric Model: 1999 Version (GRAM-99)," NASA TM-209630, May 1999.